International Symposium of Research Students on Material Science and Engineering
December 20-22, 2004, Chennai, India
Department of Metallurgical and Materials Engineering, Indian Institute of Technology Madras

SYNTHESIS, CHARACTERISATION AND ELECTRICAL TRANSPORT PROPERTIES OF MANGANITE NANOPARTICLES

C. Krishnamoorthy, K. Sethupathi and V. Sankaranarayanan.
Department of physics,Indian Institute of Technology, Chennai-600 036, India.

ABSTRACT

Nanocrystalline $La_{0.875}Sr_{0.125}MnO_3$ sample was prepared by citrate auto-ignition method. The crystal structure of the sample found to be rhombohedral with space-group $R\bar{3}c$ and the crystallite size to be 20nm. The electrical resistivity favours variable range hopping (VRH) mechanism in paramagnetic regime with magnetic localisation due to e_g and t_{2g} electrons interaction rather than conventional Anderson localisation of electrons. A linear metallic behaviour was observed in metallic regime ($T_{IM} < T < T_{MI}$). The low temperatures insulating behavior was explained by charge/orbital ordering phenomena.

1. INTRODUCTION

The discovery of colossal magnetoresistance (CMR) in the hole-doped manganese perovskites $L_{1-x}A_xMnO_3$, where L and A are trivalent lanthanide and divalent alkaline earth ions respectively, has attracted much interest because of their interesting physics and the potential for magnetoelectronic applications. Of the various manganese perovskites, the $La_{1-x}Sr_xMnO_3$ system has received a lot of interest because it has near room temperature magnetic transition temperature, T_c. Over the entire composition range, the system exhibits rich magnetic and electrical phases [1]. An additional characteristic feature of the manganites is charge ordering. In $La_{1-x}Sr_xMnO_3$ this ordering was observed by the neutron scattering as well as high energy X-ray diffraction. This ordering phenomenon found to be restricted to a small substitution regime close to the values giving a commensurate fraction of charge carriers [2-4]. Among all the compositions of the $La_{1-x}Sr_xMnO_3$, the $La_{0.875}Sr_{0.125}MnO_3$ shows a variety of structural, electrical and magnetic transitions over a range of temperatures [5].

Currently, one of the main trends in device applications is the size reduction of devices to nanoscale. It is therefore important to study the structure and physical properties of the CMR materials at such a nanoscale. The samples with smaller grain sizes possibly show richer electronic and magnetic properties, due to the influence of the structural and magnetic disorders at the grain interfaces. Thus, careful grain size control during oxide fabrication is very important. Chemical methods give the ability to produce powders with exceptionally small grain size in the nanometer range. Many authors reported the production of manganite fine powders via different routes: e.g. ball milling [6,7], urea gel complex method [8,9], Citric acid- ethylene diamine gel route [10,11], pechini method [12], molten alkali metal nitrate flux [13], PVA-based chemical synthesis route [14] and amorphous citrate method [15]. In this paper, we present the preparation of $La_{0.875}Sr_{0.125}MnO_3$ nanoparticles through citrate-gel autoignition method, modified amorphous citrate gel method, which is very much used to prepare other oxide materials.

2. EXPERIMENTAL PROCEDURES

Single phase, nanocrystalline samples of $La_{0.875}Sr_{0.125}MnO_3$ were synthesised by citrate auto-ignition method. Stoichiometric amounts of analytical grade La_2O_3, $SrCO_3$, $Mn(CH_3COO)_2$. $4H_2O$ and $C_6H_8O_7$ were used as starting materials. Before weighing, La_2O_3 was pre-fired at 1000 ^{0}C for

several hours to decompose residual carbonates and hydrates. La_2O_3, $SrCO_3$ were converted into their corresponding soluble nitrates by dissolving them in dilute HNO_3, in individual beakers. $Mn(CH_3COO)_2.4H_2O$ and citric

acid are readily soluble in water. All the metal solutions were mixed together and stirred for 5 minutes to make a homogeneous solution and then citric acid was added to it as a chelating agent and fuel. The molar ratio of [citric Acid]: [cation] is 3 and the pH of the solution was adjusted to neutral value using the aqueous NH_3 solution to avoid precipitation. The resulting solution was slowly evaporated at 80-90 ^{0}C on a hot plate. After several hours of evaporation the solution became brown coloured viscous solution and this gel was kept in a furnace at ~250 ^{0}C. After several minutes, the gel was foamed, swelled with evolving large volume of gases and then automatically ignited and burnt with glowing flints. The auto-ignition was completed within a minute yielding a highly porous black fluffy material with fine powder, called a precursor. The thermal behaviour of the precursor was determined with a NETZSCH STA 409C thermal analyser with a heating rate of 10°C/min in the temperature range 30-1000 ^{0}C. The precursor was calcined for 5h at 850 ^{0}C to produce nanoparticle sample.

The samples were structurally characterised by x-ray diffraction using a Shimadzu XD-D1 powder diffractometer in Bragg-Brentano geometry with Cu K_α radiation. The morphology and microstructure of the sample was obtained by using JSM-840 Scanning Electron Microscope. To measure the DC electrical resistivity, the powder was made pellet, sintered for 10 minutes at calcined temperature (850 ^{0}C) to make the particles welded each other without further grain growth. The electrical resistivity of the samples was measured in the temperature range 20-300 K by standard four-probe technique with the probes attached to the samples using silver paste.

3. RESULTS AND DISCUSSIONS

3.1. Thermal Analysis

Thermogravimetry analysis (TGA) and Differential Thermal Analysis (DTA) of precursor show that there were mainly three weight loss regions in the TGA curve in the temperature range ~100-720 ^{0}C, see Fig.1. The weight loss below 180 ^{0}C is ~8% and may be due to dehydration of water molecules. The weight loss between 210 and 320 ^{0}C is ~30% and is due to the decomposition of citric acid around 300 ^{0}C. The weight loss between 420-710 ^{0}C is very small and may be due to burning of residual organic compounds of the precursor and an endothermic peak is observed in DTA curve. Above 720 ^{0}C there is no weight loss in TGA curve.

3.2. Structural and morphology

Room temperature powder x-ray diffraction (XRD) profiles confirmed the pure single phase of the sample. The precursor profile shows amorphous behavior. Our experimentally obtained profiles were fitted to the theoretical powder diffraction patterns calculated using "Powder Cell 2.3" [16]. We obtain the best fit for rhombohedral structure of space-group $R\bar{3}c$. The obtained lattice and fitting parameters are a= 5.503, c= 13.337 $\overset{0}{A}$ and R_p=6.52, R_{wp}=8.25. The fitted profiles are shown in Fig.2 and the inset shows the Gaussian fit for (110) plane in XRD profile (the circles are experimental data and solid line is the fitted curve) to calculate the full width at half maxima (FWHM). The crystallite size is calculated from x-ray diffraction profiles, using Scherrer's formula [17]

$$D = \frac{0.9\lambda}{\beta \mathrm{Cos}\theta},$$

where $\beta^2 = (\mathrm{FWHM})^2_{\mathrm{nanopowder}} - (\mathrm{FWHM})^2_{\mathrm{Bulksample}}$, the $(\mathrm{FWHM})_{\mathrm{Bulk\ sample}}$ gives the instrumental broadening and β in radians, θ - centre of the peak, λ - wavelength of the X-ray used. The

crystallite size calculated using the above formula to be 20nm. Fig.3 shows the SEM micrograph obtained for this nanocrystalline sample. The photograph shows that the particles are spherical in shape and more or less homogeneously distributed. The average particle size measured from the SEM photograph using GIMP software is 64nm. The measured particle size is deviating from crystallite size, calculated from XRD profile.

This can be understood by take into account that one particle may consist of more than one crystallite, called polycrystallite particle, the later is observed by X-rays while the former is observed by SEM. Twinning and other structural defects (vacancies, dislocations) can explain the presence of the crystallite domains in the particle [20]. To confirm the exact morphology of the individual particle or further low dimensional morphology analysis we need have to do high resolution TEM (HRTEM).

3.2 Electrical resistivity

Hole doped manganites shows very interesting electronic transport behavior viz., insulator to metal transition, the decrease of resistance upon application of magnetic field (negative magnetoresistance). It is interesting to study the mechanism of transport in these materials, especially in nanocrystalline material. The electrical resistivity of the sample shows two distinct transitions as a function of temperature and is shown in Fig.4.

As we decrease the temperature, the samples shows a clear transition from an insulating to a metallic state at the temperature (~100K), generally referred to the insulator-metal transition temperature (T_{IM}). At temperature below 42 K the sample shows an insulating behaviour (see inset of Fig.4) and the on-set of this behavior is denoted here as $T_{metal\text{-}insulator}$ (T_{MI}). This temperature may mark the onset of charge and/or orbital ordering in this sample.

In order to understand the electronic transport mechanism in these compounds, resistivity data have been analyzed separately corresponding to insulating ($T > T_{IM}$), metallic ($T_{IM} < T < T_{MI}$) and low temperature insulating ($T < T_{MI}$) regimes. The electronic conduction in the paramagnetic regime ($T > T_{IM}$) is usually explained in terms of either variable range hopping (VRH) or the polaronic models. We have plotted $\ln[\rho(T)]$ as a function of T^n, where n= -1, –1/2 and –1/4. The T^{-1} law, which would be characteristic of nearest-neighbor hopping, activation to mobility edge or narrow gap semiconduction, does not fit the data. A $T^{-1/2}$ law, characteristic of variable range hopping (VRH) with a soft gap due to electron correlation, gives a satisfactory fit. The $T^{-1/4}$ law, which is also characteristic of VRH [18], gives a good fit in the paramagnetic regime, in any case supporting the VRH model as the mechanism for current transport in the paramagnetic regime above the metal-insulator transition.

In the original Mott model of variable range hopping (VRH) among Anderson localized states,

$$\rho(T) = \rho_\infty \exp(T_0 / T)^{1/4} \text{-------(1)}$$

where ρ_∞ depends on the phonon density because the hopping is phonon-assisted and the characteristic of temperature T_0 depends on the localization length $1/\alpha$ of the electrons and the density of states $N(E_F)$

$$k T_0 = 18\alpha^3 / N(E_F) \text{ ----------(2).}$$

Hopping distance R and hopping energy W were calculated by using

$$R^4 = 9/[8\pi\alpha kTN(E_F)] \text{ and } W = 3/[4\pi R^3 N(E_F)] \text{ -----------(3)}$$

respectively. Electron hopping is always of variable-range type at low temperature where the thermal energy is not great enough to allow electrons to hop to their nearest neighbor high energy states. In that case it is more favorable for electrons to hop farther to find a smaller potential difference. At high temperatures, conduction may be by activation above the mobility edge. In the

intermediate range, nearest-neighbor hopping can contribute significantly to the transport. Fig.5 shows $\ln[\rho(T)]$ as a function of $T^{-1/4}$ [Eq. (1)] and the T_0 value obtained from the fit is 3.2889×10^7. To interpret the data above Curie-temperature Tc, in terms of this model, we need the electronic density of states (DOS) $N(E_F)$. Coey et.al [19] reported the density of states from low temperature heat capacity measurements for $La_{0.7}Sr_{0.3}MnO_3$ is 4×10^{28} $m^{-3}eV^{-1}$. The number of e_g electrons is $0.7/v = 1.2 \times 10^{28}$ m^{-3}, and hence the occupied part of the e_g band is about 0.3eV wide. Values of kT_0 (Fig.5) is 2834 eV and the corresponding localization length deduced from eq.(2) is 0.0541 nm. At room temperature, the value of average hopping distance R [eq. (3)] is 0.37 nm. Since the localization length must exceed the Mn ion radius (0.07 nm) and the hopping distance should exceed the Mn-Mn distance (0.55 nm), the obtained values are not compatible with conventional variable-range hopping.

This unphysical result underlines a fundamental problem: either the density of states decreases drastically above Tc, or else the localization mechanism is different. Manganites with x= 0.3 show a little structural change at Tc, so that any changes in band structure and density of states should be associated with the onset of ferromagnetic order. In order to get compatible values of localization length and hopping distance, from Mott's theory, Viret et.al [20] proposed that random potential of mainly magnetic origin, in addition to other potentials (grain boundary etc.,), is responsible for carrier localization above Tc. This potential is due to Hund's-rule coupling between localized Mn t_{2g} ion cores (S= 3/2) and the spins (s) of the e_g electrons in the σ^* conduction band. The authors were able to deduce the following equation to estimate the density of states

$N(E_m) = p(E_m)(1-x)\,\phi\, g/v$ ---------(4).

where $(1-x) = 0.125$ is the probability that the e_g orbital at the manganese site receiving the hopping electron is uncoupled, ϕ is geometric factor of order of 0.5 and g is the probability that an unoccupied manganese orbital can actually accept an electron. When divalent concentration, x= 0.3, the g factor in three dimensions is approximately 0.875. Hence the value of $N(E_m)$ deduced from Eq.(4) is 9.37×10^{26} $m^{-3}eV^{-1}$. Using this N(E) values, the localization length of the sample is 0.19 nm and the average hopping distance at room temperature is 1.31 nm. The hopping energy at room temperature is $\Delta E \approx 0.12$ eV. These values are physically plausible since the localization length exceeds the ionic radius of Mn^{3+} and the hopping distances are 2-3 times the Mn-Mn separation.

The intermediate metallic behavior ($d\rho/dT > 0$) occurs between T_{IM} and T_{MI} as seen in the single and bulk polycrystalline samples. The resistivity shows a linear dependence on the temperature in this regime (see Fig.5), over 40K, is characteristic of pure metal (e.g., Cu).

The low-temperature transition at T_{CO} to an insulating state in the resistivity plot has been observed in single crystals as well as polycrystalline samples of this composition [5,21]. However one major difference is that this transition is observed at 140 K (T_{CO}) for single crystals and bulk polycrystalline samples while it occurs at about 45 K for our nanoparticle sample. This phase is referred in most cases as the charge/orbital ordered phase. Super exchange interaction is the origin of ferromagnetism in this phase. In polycrystalline samples, along with charge ordering, the grain boundary contribution results in a small Coulomb barrier of electrostatic origin at low temperature. This can also cause this low temperature insulating state, in addition to charge/orbital order. Balcell et.al. [6] reported that this low temperature insulating behavior in resistivity occurs for the small (metallic) grains and $\ln(\rho)$ scales as $T^{-1/2}$. This behavior was predicted by assuming the nanoparticle core is in metallic state and the outer layer (shell) is in an amorphous/insulating state by resembling the metal fine particles in an insulating matrix, which was well studied in early 1970's [22]. In the present study, the sample is expected to be an insulating state at low temperature due to charge ordered phenomenon in this composition. Even though the $\ln(\rho)$ scales very well with $T^{-1/2}$ at low temperatures, the above mentioned $\ln(\rho)$ vs. $T^{-1/2}$ explanation may not be applicable here since the nanoparticle cores are in insulating state, as should be due to charge order. Thus we will assume that the low temperature insulating state originated by charge ordering of e_g electrons of Mn^{3+} but the T_{CO} shifted to very low temperatures (45 K). One interesting feature is that the low temperature

insulating values vary very slowly compared with the bulk sample's exponential variation. In order to probe this feature we have to perform neutron diffraction or high-energy X-ray diffraction measurements.

4.CONCLUSIONS

We have successfully prepared nanocrystalline $La_{0.875}Sr_{0.125}MnO_3$ sample of grain size 20 nm by citrate-autoignition method. The thermal analysis shows that the citric acid completely decomposes around 710 ^{0}C. The particles are in spherical in shape and more or less homogeneously dispersed. The electrical resistivity shows variable range hopping (VRH) mechanism is the favourable one in paramagnetic regime with a magnetic localisation mechanism due to e_g and t_{2g} electron interaction of Mn rather than Anderson localisation. At low temperature the sample shows an insulating behaviour, this may be due to charge/orbital ordering.

5. REFERENCES

1). Nanoscale phase separation and colossal magnetoresistance: The physics of manganites and related compounds edited by E. Dagotto, 2003 (Springer-Verlag, Berlin).
2] C. H. Chen and S-W. Cheong, Phys. Rev. Lett. **7**6, (1996). 4042
3] P. G. Radaelli, D.E. Cox, M.Marezio, S-W. Cheong, Phys. Rev. B **5**5, (1997) 3015 .
4] Y. Tokura, H. Kuwahara, Y. Moritomo, Y. Tomioka, A. Asamitsu, Phys. Rev. Lett. **7**6 (1996) 3184.
5] M. Paraskevopoulos, F. Mayr, C. Hartinger, A. Pimenov, J. Hemberger, P. Lunkenheimer, A. Loidl, A.A. Mukhin, V.Y. Ivanov " , A.M. Balbashov, J. Magn. Magn. Mater. 211 (2000) 118.
6] Ll. Balcells, J. Fontcuberta, B. Martinez, X. Obradors, Phys. Rev. B **58** (1998) R14697.
7] Run-Wei Li, Han Xiong, Ji-Rong Sun, Qing-An Li, Zhi-Hong Wang, Jian Zhang, Bao-Gen Shen, J. Phys: Conden. Matter. **13**(2001)141.
8]. C. Vazquez-Vazquez, M. Carmen Blanco, M. Arturo Lopez-Quintela, R.D. Sanchez, J. Rivas, S.B. Oseroff, J. Mater. Chem**. 8**(1998)991.
9]. J. Rivas, L.E. Hueso, A. Fondado, F. Rivadulla and M.A. Lopez-Quintela, J. Magn. Magn. Mater. **221**(2000)57.
10] R. Mahendiran, R. Ramesh, A.K. Raychaudhuri, C.N.R. Rao Solid Stat. Commun. **99**(1996)149.
11]. R. Mahesh, R. Mahendran, A.K. Raychoudhuri, C.N.R.Rao, Appl. Phys. Lett. **68**(1996)2291.
12] M. Gaudon, C. Laberty-Robert, F. Ansart , P. Stevens, A. Rousset, Solid State Sciences **4** (2002) 125
13] Feng Luo, Yun-Hui Huang, Chun-Hua Yan, Shan Jiang, Xiao-Hang Li, Zhe-Ming Wang, Chun-Sheng Liao, J. Magn. Magn. Mater. **260** (2003) 173.
14]. Dinesh K. Pandya , Subhash C. Kashyap, Gyana R. Pattanaik, J. of Alloys and Compounds **326** (2001) 255.
15] P.Courty, H. Ajot, C. Marcilly, Powder Tech. 7 (1973)21.
16] W.Kraus, G.Nolze, J.Appl. Cryst. **29**(1996)301.
17] X-ray diffraction procedures for Polycrystalline and Amorphous Materials, H.P. Klug, L.E. Alexander, 1974 (John Wiley, NY).
18] Metal-Insulator transitions, N.F. Mott (Taylor & Francis, 1990).
19] J. M. D. Coey, M. Viret, and L. Ranno, K. Ounadjela, Phys. Rev. Lett. 75(1995)3910.
20] M. Viret, L. Ranno, and J. M. D. Coey, Phys. Rev. B **55** (1997) 8067.
21] S. Uhlenbruck, R. Teipen, R. Klingeler, B. Büchner, O. Friedt, M. Hücker, H. Kierspel, T. Niemöller, L. Pinsard, A. Revcolevschi, and R. Gross, Phys. Rev. Lett. 82 (1999) 185.
22] B. Abeles, P.Sheng, M.D. Coutts, Y.Arie, Adv. Phys. 24 (1975)407.

FIGURES

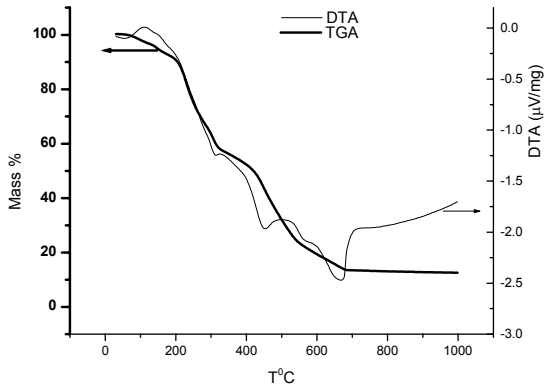

Fig.1: The thermogravimetry analysis (TGA and DTA) of $La_{0.875}Sr_{0.125}MnO_3$. The thick line shows weight loss and the thin line shows DTA curve.

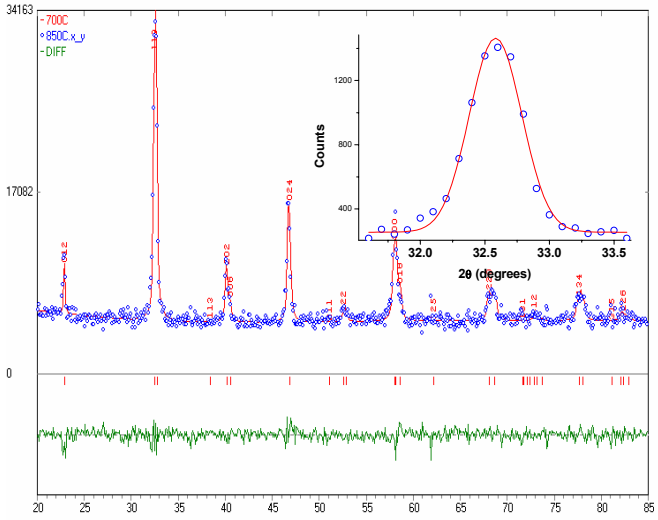

Fig.2: Rietveld fitted X-ray diffraction profiles. The inset shows Gaussian fit for (110) plane to calculate FWHM. The circles are data points and solid line is theoretical curve.

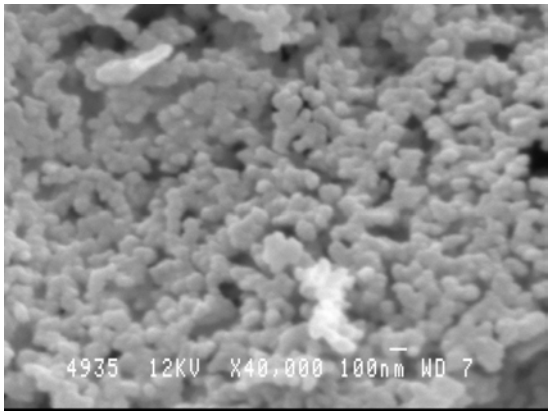

Fig.3: SEM micrograph of $La_{0.875}Sr_{0.125}MnO_3$

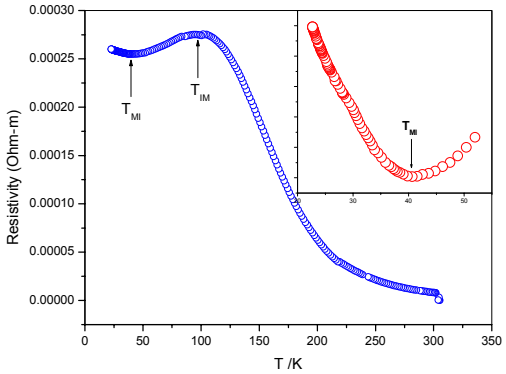

Fig.4: The electrical resistivity as a function of temperature. The inset shows the enlarged low temperature insulating region.

.

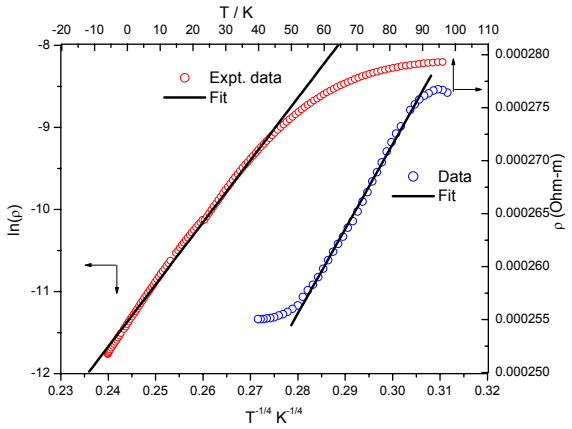

Fig.5: The fitted curves of resistivity. The left hand scale shows VRH model and the right hand scale shows linear metallic behavior